= 0.9, 0.8, and 0.7. For example, we obtain $F = 1 - 10^{-5}$ after $N = 12$ steps for $\pi_+ = 0.9$. For general channels the fidelity approaches $F \sim 1 - e^{-cN}$, with N the number of steps. We emphasize that for $\pi_+ = 1$ we have a stationary channel. In this case, we obtain $F_1 = 1$ in a single step.

For a "good" standard channel (see Eq. 3), T_0 is close to T_1. As a consequence of our reduction procedure, this implies that $S_0 \simeq S_1$ and therefore $\pi_+ \simeq 1$, and $\pi_- \ll 1$. We emphasize that the reverse statement is not true; namely, one can have $S_0 \simeq S_1$ but a "bad" standard channel. Consider, for example, a very simple toy model in which the environment is a qubit in the initial state $|0\rangle$, and with $T_0 = \mathbb{1}$ and $T_1 = \sigma_x$. With the classical definition of a channel, one can easily show that this channel cannot produce entanglement; suppose that Alice has an entangled state of two qubits A and A_2, $|\alpha\rangle_A|0\rangle_{A_2} + |\beta\rangle_A|1\rangle_{A_2}$, and sends the second qubit to the qubit B of Bob via such a channel. The state after this transmission will be a mixed state $|\alpha\rangle_A\langle\alpha\|0\rangle_B\langle 0| + \langle\beta\rangle_A\langle\beta\|1\rangle_B\langle 1\rangle$ and therefore is not entangled. However, for this channel $S_0 = S_1 = \sigma_x$, and therefore one can establish an EPR pair with the procedure introduced above. By twice using the channel as we proposed, the state of the environment after both transmission factorizes out, and therefore entanglement can be produced. When $S_0 \simeq S_1$, then $\pi_- \propto \|(S_0 - S_1)|E\rangle\|^2 \approx 0$, which is due to quantum interference between the first and second transmission, using the reduction scheme of Eq. 4.

We have defined a photonic channel where $|0\rangle$ is assigned to sending no photon and $|1\rangle$ is assigned to sending one photon. Using local quantum computing with three and two auxiliary atoms in the first and second node, we have reduced it to an absorption-free channel. We have proposed a scheme based on this channel that iteratively improves the fidelity of distant EPR pairs, using quantum interference between two transmissions. For a stationary channel, one obtains a pure EPR pair in a single step. For a general channel, the fidelity approaches 1 exponentially with the number of steps.

REFERENCES AND NOTES

1. W. K. Wootters and W. H. Zurek, *Nature* **299**, 802 (1982).
2. C. H. Bennett, *Phys. Today* **48** (no. 1), 24 (1995).
3. C. H. Bennett *et al.*, *Phys. Rev. Lett.* **76**, 722 (1996); A. Ekert and C. Macchiavello, *ibid.* **77**, 2585 (1996).
4. P. W. Shor, *Phys. Rev. A* **52**, 2493 (1995); A. M. Steane, *Phys. Rev. Lett.* **77**, 793 (1996); E. Knill and R. Laflamme, *Phys. Rev. A* **55**, 900 (1997); J. I. Cirac, T. Pellizzari, P. Zoller, *Science* **273**, 1207 (1996).
5. J. I. Cirac, P. Zoller, H. Mabuchi, H. J. Kimble, *Phys. Rev. Lett.* **78**, 3221 (1997).
6. S. J. van Enk, J. I. Cirac, P. Zoller, *Phys. Rev. Lett.* **78**, 4293 (1997).
7. See, for example, B. Schumacher, *Phys. Rev. A* **45**, 2614 (1996); C. H. Bennett, D. P. DiVincenzo, J. A. Smolin, *Phys. Rev. Lett.* **78**, 3217 (1997).
8. C. H. Bennett *et al.*, *Phys. Rev. Lett.* **70**, 1895 (1993).
9. One can also use repumping techniques to supply fresh ancillas in error correction and purification. However, one still needs an infinite number to correct all errors.

10. This work was supported in part by the TMR network ERB-FMRX-CT96-0087 and by the Austrian Science Foundation.

2 July 1997; accepted 12 November 1997

A Laser Ablation Method for the Synthesis of Crystalline Semiconductor Nanowires

Alfredo M. Morales and Charles M. Lieber*

A method combining laser ablation cluster formation and vapor-liquid-solid (VLS) growth was developed for the synthesis of semiconductor nanowires. In this process, laser ablation was used to prepare nanometer-diameter catalyst clusters that define the size of wires produced by VLS growth. This approach was used to prepare bulk quantities of uniform single-crystal silicon and germanium nanowires with diameters of 6 to 20 and 3 to 9 nanometers, respectively, and lengths ranging from 1 to 30 micrometers. Studies carried out with different conditions and catalyst materials confirmed the central details of the growth mechanism and suggest that well-established phase diagrams can be used to predict rationally catalyst materials and growth conditions for the preparation of nanowires.

One-dimensional (1D) structures with nanometer diameters, such as nanotubes and nanowires, have great potential for testing and understanding fundamental concepts about the roles of dimensionality and size in, for example, optical, electrical, and mechanical properties and for applications ranging from probe microscopy tips to interconnections in nanoelectronics (*1*). The synthesis of crystalline semiconductor nanowires, such as Si and Ge (*2*), holds considerable technological promise for device applications and for improving the optical properties of these indirect gap materials but has been difficult to achieve. Several successful routes for the synthesis of carbon nanotubes are known (*3*), but the different bonding arrangement within these nanotubes and the different chemistry of carbon compared with Si and Ge would require an alternative approach for controlling the formation of nanowires from gas-phase reactants. Template-mediated methods that use zeolites, membranes, or nanotubes (*4*) can control growth but usually form polycrystalline materials.

An approach that does form crystalline wirelike structures is VLS growth (*5*, *6*), in which a liquid metal cluster or catalyst acts as the energetically favored site for absorption of gas-phase reactants. The cluster supersaturates and grows a 1D structure of the material; the lower limit of the diameter is generally >0.1 μm and is limited by the minimum diameter of the liquid metal catalysts that can be achieved under equilibrium conditions (*6*). A VLS method has been used to grow Si nanowires by confinement of Au metal on a surface (*7*, *8*), although the smallest diameters (20 to 100 nm) of defect-free nanowires are still relatively large. Recently, Buhro and co-workers have reported a promising solution-liquid-solid (SLS) synthesis of 10- to 100-nm-diameter III-V semiconductors (*9*). A potential limitation of the SLS approach, however, is the requirement of a catalyst that melts below the solvent boiling point.

We report an approach to the synthesis of single-crystal nanowires that exploits laser ablation to prepare nanometer-diameter catalyst clusters that subsequently define the size of wires produced by a VLS mechanism. This approach to generating nanometer-diameter clusters is understood from previous studies (*10*, *11*), and it overcomes the limitation of equilibrium cluster sizes in determining minimum wire diameters. We demonstrated this method with the synthesis of single-crystal Si and Ge nanowires with diameters as small as 6 and 3 nm, respectively, and lengths >1 μm. Because equilibrium phase diagrams can be used to rationally choose catalyst materials and growth conditions (*6*) and laser ablation can be used to generate nanometer-sized clusters of virtually any material, we believe that our approach could be adapted for preparing nanowires of numerous materials.

A. M. Morales, Department of Chemistry and Chemical Biology, Harvard University, Cambridge, MA 02138, USA.
C. M. Lieber, Department of Chemistry and Chemical Biology, and Division of Engineering and Applied Sciences, Harvard University, Cambridge, MA 02138, USA.

*To whom correspondence should be addressed. E-mail: cml@cmliris.harvard.edu

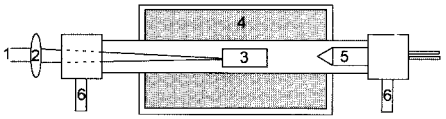

Fig. 1. Schematic of the nanowire growth apparatus. The output from a pulsed laser (1) is focused (2) onto a target (3) located within a quartz tube; the reaction temperature is controlled by a tube furnace (4). A cold finger (5) is used to collect the product as it is carried in the gas flow that is introduced (6, left) through a flow controller and exits (6, right) into a pumping system.

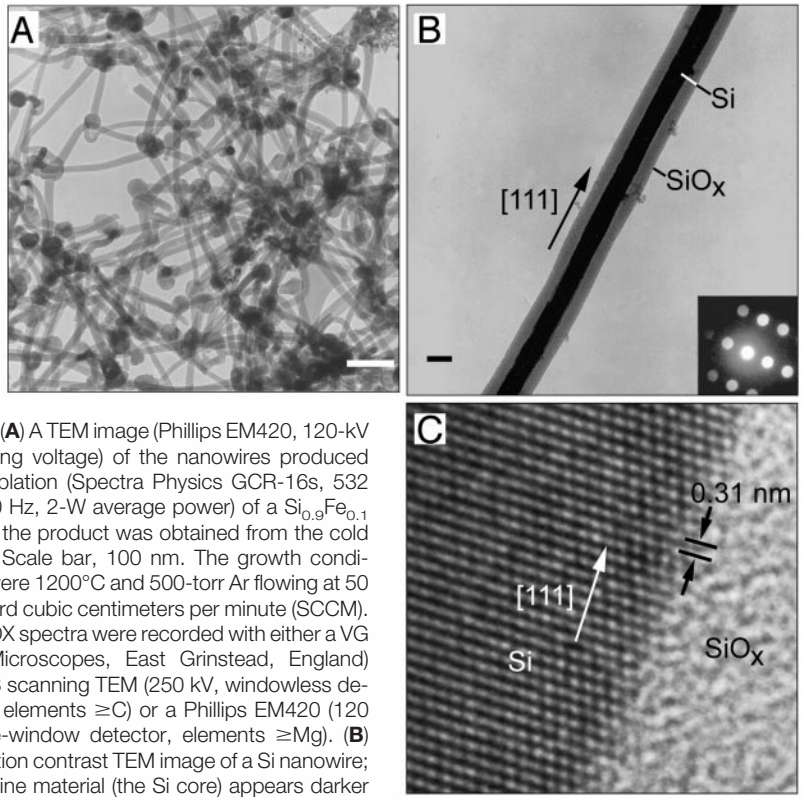

Fig. 2. (**A**) A TEM image (Phillips EM420, 120-kV operating voltage) of the nanowires produced after ablation (Spectra Physics GCR-16s, 532 nm, 10 Hz, 2-W average power) of a $Si_{0.9}Fe_{0.1}$ target; the product was obtained from the cold finger. Scale bar, 100 nm. The growth conditions were 1200°C and 500-torr Ar flowing at 50 standard cubic centimeters per minute (SCCM). The EDX spectra were recorded with either a VG (VG Microscopes, East Grinstead, England) HB603 scanning TEM (250 kV, windowless detector, elements ≥C) or a Phillips EM420 (120 kV, Be-window detector, elements ≥Mg). (**B**) Diffraction contrast TEM image of a Si nanowire; crystalline material (the Si core) appears darker than amorphous material (SiO_x sheath) in this imaging mode. Scale bar, 10 nm. (**Inset**) Convergent beam ED pattern recorded along the [211] zone axis perpendicular to the nanowire growth axis. (**C**) High-resolution TEM image [Topcon (Topcon Technology, Tokyo, Japan) EM-002B, 200-kV operating voltage] of the crystalline Si core and amorphous SiO_x sheath. The (111) planes (black arrows) (spacing, 0.31 nm) are oriented perpendicular to the growth direction (white arrow).

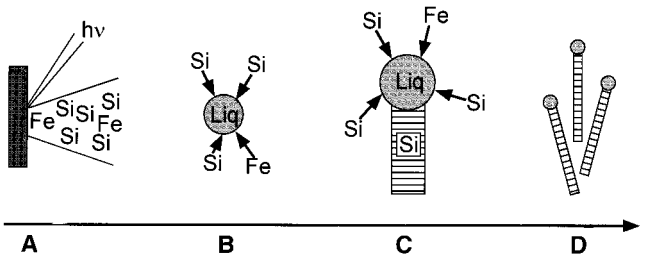

Fig. 3. Proposed nanowire growth model. (**A**) Laser ablation with photons of energy $h\nu$ of the $Si_{1-x}Fe_x$ target creates a dense, hot vapor of Si and Fe species. (**B**) The hot vapor condenses into small clusters as the Si and Fe species cool through collisions with the buffer gas. The furnace temperature (Fig. 1A) is controlled to maintain the Si-Fe nanocluster in a liquid (Liq) state. (**C**) Nanowire growth begins after the liquid becomes supersaturated in Si and continues as long as the Si-Fe nanoclusters remain in a liquid state and Si reactant is available. (**D**) Growth terminates when the nanowire passes out of the hot reaction zone (in the carrier gas flow) onto the cold finger and the Si-Fe nanoclusters solidify.

In our growth apparatus (Fig. 1), a pulsed, frequency-doubled Nd–yttrium-aluminum-garnet laser (wavelength, 532 nm) is used to ablate targets that contain the element desired in the nanowire and the metal catalyst component. This target was located within a quartz furnace tube in which the temperature, pressure, and residence time can be varied. A transmission electron microscope (TEM) image of a typical Si nanowire product (Fig. 2A) obtained after laser ablation of a $Si_{0.9}Fe_{0.1}$ target at 1200°C shows primarily wirelike structures with remarkably uniform diameters on the order of 10 nm (*12*) with lengths >1 μm and often as large as 30 μm. Electron-induced x-ray fluorescence (EDX) analysis of individual nanowires showed that they contain only Si and O. In addition, the TEM images show that virtually all of the nanowires terminate at one end in nanoclusters with diameters 1.5 to 2 times that of the connected nanowire. The observation of nanocluster spheres at the ends of the nanowires is suggestive of a VLS growth process (see below).

Higher resolution TEM images recorded on individual nanowires (Fig. 2, B and C) provide further insight into the structure of these materials. A diffraction contrast image shows that the nanowires consist of a very uniform diameter crystalline core surrounded by an amorphous coating (Fig. 2B). The average diameter of the crystalline core of this nanowire is 7.8 ± 0.6 nm, and the total diameter including the amorphous sheath is 17.1 ± 0.3 nm. Analysis of images taken from a number of Si nanowires grown under similar conditions showed that the diameters of the crystalline cores vary from 6 to 20 nm with an average close to 10 nm. A convergent beam electron diffraction (ED) pattern recorded perpendicular to the nanowire long axis (Fig. 2B) could be indexed for the [211] zone axis of crystalline Si and suggests that the nanowire growth occurs along the [111] direction. This direction was confirmed in lattice-resolved TEM images of the crystalline core (Fig. 2C). Such images clearly show the (111) atomic planes (separation, 0.314 nm) perpendicular to the nanowire axis (*13*), and an atomically sharp interface with the amorphous coating. Electron-induced x-ray fluorescence analysis with a scanning TEM showed that the amorphous coating has an approximate composition of SiO_2. We attribute the amorphous SiO_2 coating on the nanowires to reaction with residual oxygen in the apparatus. As expected for SiO_2, hydrofluoric acid removed the amorphous nanowire coating, and subsequent EDX analysis of the bare crystalline cores showed only Si with traces of oxygen. Taken together, these structure and composition data show that the nanowires produced with our laser-based method consist of 6- to 20-nm-diameter crystalline Si cores that grow along the [111] direction and are sheathed by amorphous SiO_2.

Further advancement of this approach to nanowire synthesis requires a clear understanding of the growth mechanism. The presence of nanoparticles at one end of nearly all of the nanowires qualitatively suggests that our growth proceeds by a VLS mechanism. This idea can be tested and developed in more detail by consideration of the model in Fig. 3. In this model, laser ablation of the $Si_{1-x}Fe_x$ target produces a vapor of Si and Fe (Fig. 3A) that rapidly condenses into Si-rich liquid nanoclusters (Fig. 3B), and when the nanoclusters become supersaturated, the co-

existing Si phase precipitates and crystallizes as nanowires (Fig. 3C). Ultimately, the growth terminates when the gas flow carries the nanowires out of the hot zone of the furnace (Fig. 3D). This model can be used to make several testable predictions in conjunction with the binary Si-Fe phase diagram (*14*). First, we expect that the terminating solid nanoclusters are $FeSi_2$; that is, $FeSi_2$ is the stable Fe-Si compound in the Si-rich region of the phase diagram. Second, we expect that nanowire growth will terminate below 1207°C, because no liquid cluster would remain [this temperature corresponds to the isotherm separating $FeSi_x(l) + Si(s)$ from $FeSi_2(s) + Si(s)$].

Our experimental results are in good agreement with these predictions. Quantitative EDX analysis of the clusters at the ends of the nanowires showed that these clusters have the expected $FeSi_2$ composition, and EDX measurements made on the nanowires a short distance from the $FeSi_2$ nanoclusters also showed that no Fe is detected at the 1 atomic % sensitivity level of our instrument. In addition, TEM images of these nanoclusters show atomic planes separated by 0.51 nm. This separation agrees well with the 0.510-nm distance between (001) planes in β-$FeSi_2$ (*15*). Finally, the growth of the Si nanowires occurred only for temperatures greater than 1150°C with the Fe catalyst. The observation of Si nanowire growth at temperatures below the bulk solidus line at 1207°C is reasonable, because the melting points of nanoclusters are lower than the corresponding bulk solids (*16*).

The good agreement between the experimental data and the predictions of our model suggests that it should be possible to rationally choose new catalysts and growth conditions for nanowire synthesis. Examination of binary Si-metal phase diagrams (*14*) showed that, like Si-Fe, Si-Ni and Si-Au exhibit eutectic Si-rich regions with Si as the primary solid phase. Laser vaporization of Si targets containing either 10% Ni or 1% Au produced Si nanowires that have the same structural characteristics as those described above for the Si-Fe systems. In addition, virtually all of the Si nanowires produced with the Ni and Au catalysts terminated in β-$NiSi_2$ and Au nanoclusters, respectively (*17*). These data thus provide strong support for the generality of our approach. Gold has been used in the past as a VLS catalyst for Si growth, primarily on surfaces (*6*, *8*, *18*), although to the best of our knowledge a direct growth of single-crystal Si nanowires ≤10 nm diameter has not been reported (*19*).

In addition, we made a more stringent test of our approach by preparing Ge nanowires. Examination of the Ge binary phase diagrams showed that the Ge-rich region of the Ge-Fe diagram is similar to that of the Si-Fe diagram (*14*); that is, the phases above 838°C are $FeGe_x(l) + Ge(s)$, and below this temperature they are β-$FeGe_2(s) + Ge(s)$. Hence, the major difference between Ge-Fe and Si-Fe is that the solidus line lies about 400°C lower in the former. Laser ablation of a $Ge_{0.9}Fe_{0.1}$ target at 820°C produced a good yield of wirelike products with diameters between 3 and 9 nm (Fig. 4), and TEM images show that these nanowires are crystalline, have uniform diameters without an amorphous coating, and terminate in nanoclusters. Electron-induced x-ray fluorescence analysis further demonstrated that the nanowires consist primarily of Ge and that the nanoclusters have the expected $FeGe_2$ composition. In addition, high-resolution images clearly show the Ge(111) planes and thus confirm the crystalline nature of the nanowires (Fig. 4C). The high-resolution images also exhibit twinning of the Ge(111) planes, in contrast to the results obtained for Si nanowires. At present, we do not understand the origin of twinning in the Ge nanowires, although we note that extensive twinning has been observed previously in Ge nanowires produced by a low-temperature solution synthesis (*20*).

The above studies illustrate the potential of our approach for the synthesis of crystalline nanowires. In short, a good starting point for the synthesis of nanowires of a specific composition should be an alloy that has an eutectic region with the specific material of interest. The composition of the target and laser vaporization and condensation conditions can then be adjusted to place the system in the region of the phase diagram, where the nanowire material is the primary solid phase as the temperature drops toward the solidus line or temperature at which the nanocluster solidifies. For example, it should be possible to make nanowires of SiC, GaAs, Bi_2Te_3, and BN in this way and perhaps, in the presence of atomic hydrogen, even diamond nanowires. Finally, we recently used laser ablation to produce the nanocluster catalysts separately from a gas-phase Si reactant, thus enabling greater control of the nanowire growth process (*21*).

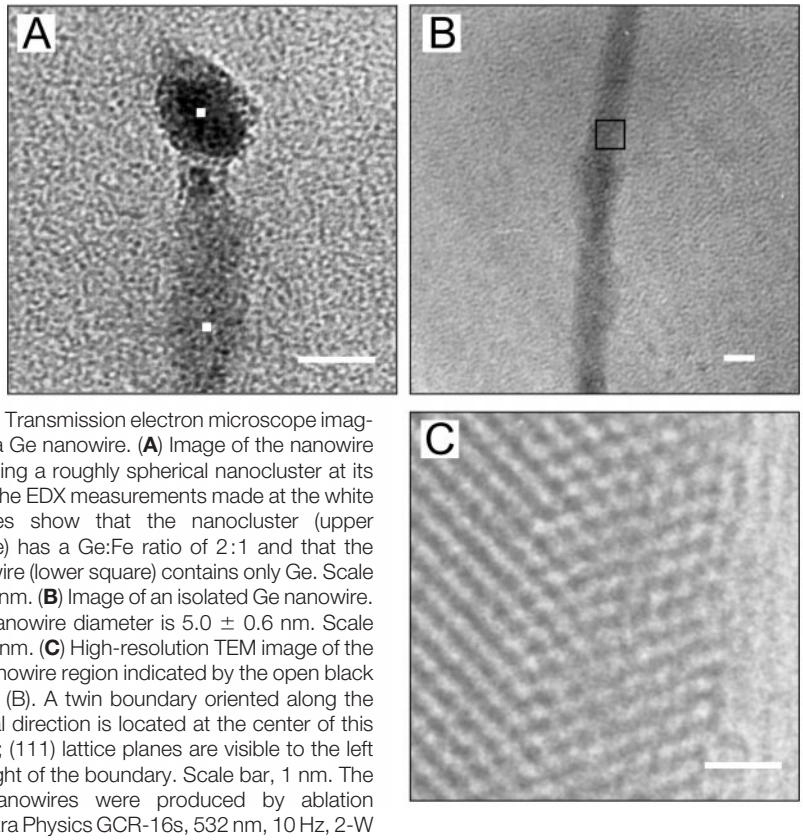

Fig. 4. Transmission electron microscope images of a Ge nanowire. (**A**) Image of the nanowire exhibiting a roughly spherical nanocluster at its end. The EDX measurements made at the white squares show that the nanocluster (upper square) has a Ge:Fe ratio of 2:1 and that the nanowire (lower square) contains only Ge. Scale bar, 9 nm. (**B**) Image of an isolated Ge nanowire. The nanowire diameter is 5.0 ± 0.6 nm. Scale bar, 5 nm. (**C**) High-resolution TEM image of the Ge nanowire region indicated by the open black box in (B). A twin boundary oriented along the vertical direction is located at the center of this image; (111) lattice planes are visible to the left and right of the boundary. Scale bar, 1 nm. The Ge nanowires were produced by ablation (Spectra Physics GCR-16s, 532 nm, 10 Hz, 2-W average power) of a $Ge_{0.9}Fe_{0.1}$ target. The growth conditions were 820°C and 300-torr Ar flowing at 50 SCCM.

REFERENCES AND NOTES

1. A. P. Alivisatos, *Science* **271**, 933 (1996); B. I. Yakobson and R. E. Smalley, *Am. Sci.* **85**, 324 (1997).
2. L. E. Brus, *J. Phys. Chem.* **98**, 3575 (1994); L. E. Brus *et al.*, *J. Am. Chem. Soc.* **117**, 2915 (1995); A. J. Read *et al.*, *Phys. Rev. Lett.* **69**, 1232 (1992); F. Buda, J. Kohanoff, M. Parrinello, *ibid.*, p. 1272; G. D. Saunders and Y.-C. Chang, *Phys. Rev. B* **45**, 9202 (1992).
3. D. T. Colbert *et al.*, *Science* **266**, 1218 (1994); J.-C. Charlier, A. De Vita, X. Blase, R. Car, *ibid.*, **275**, 647 (1997); A. Thess *et al.*, *ibid.* **273**, 483 (1996); S. Iijima and T. Ichihashi, *Nature* **363**, 603 (1993); D. Bethune *et al.*, *ibid.*, p. 605.
4. C. R. Martin, *Science* **266**, 1961 (1994); T. M. Whit-

ney, J. S. Jiang, P. C. Searson, C. L. Chien, *ibid.* **261**, 1316 (1993); C.-G. Wu and T. Bein, *ibid.* **266**, 1013 (1994); H. Dai, E. W. Wong, Y. Z. Lu, S. Fan, C. M. Lieber, *Nature* **375**, 769 (1995); E. W. Wong, B. W. Maynor, L. D. Burns, C. M. Lieber, *Chem. Mater.* **8**, 2041 (1996); C. M. Lieber, A. M. Morales, P. E. Sheehan, E. W. Wong, P. Yang, in *The Robert A. Welch 40th Conference on Chemical Research: Chemistry on the Nanometer Scale*, R. A. Welch Foundation, Houston, TX, 21 to 22 October 1996 (R. A. Welch Foundation, Houston, TX, 1996), pp. 165–187.
5. R. S. Wagner and W. C. Ellis, *Appl. Phys. Lett.* **4**, 89 (1964).
6. R. S. Wagner, in *Whisker Technology*, A. P. Levitt, Ed. (Wiley-Interscience, New York, 1970), pp. 47–119.
7. M. Yazawa, M. Koguchi, A. Muto, M. Ozawa, K. Hiruma, *Appl. Phys. Lett.* **61**, 2051 (1992).
8. J. Westwater, D. P. Gosain, S. Tomiya, S. Usui, H. Ruda, *J. Vac. Sci. Technol. B* **15**, 554 (1997).
9. T. J. Trentler *et al*., *Science* **270**, 1791 (1995).
10. T. Dietz, M. Duncan, M. Liverman, R. E. Smalley, *J. Chem. Phys.* **73**, 4816 (1980).
11. For a recent review, see M. S. El-Shall and A. S. Edelstein, in *Nanomaterials: Synthesis, Properties and Applications*, A. S. Edelstein and R. C. Cammarata, Eds. (Institute of Physics, Philadelphia, PA, 1996), pp. 13–54.
12. Analysis of the images suggests that the nanowires correspond to at least 50% of the total product. The remainder of the product corresponds to clusters containing Si, Fe, and O.
13. Analysis of the high-resolution images shows that the Si(111) planes may be oriented from 90° to 85° relative to the growth axis.
14. W. G. Moffatt, *The Handbook of Binary Phase Diagrams* (Genium, Schenectady, NY, 1976).
15. The observed β form of $FeSi_2$ is the high-temperature crystal polytype. We believe that this crystal form is kinetically trapped when the nanowire growth is terminated by quenching on the cold finger.
16. A. N. Goldstein, C. M. Echer, A. P. Alivisatos, *Science* **256**, 1425 (1992).
17. In the case of Au-catalyzed growth, Si was not detected at the 1% level in the Au nanoclusters that terminate the Si nanowires. This observation shows that compound formation (for example, $FeSi_x$ or $NiSi_x$) is not necessary for nanowire growth.
18. E. I. Givargizov, *J. Cryst. Growth* **31**, 20 (1975); G. A. Bootsma and H. J. Gassen, *ibid.*, **10**, 223 (1971).
19. Si nanowires with 10- to 25-nm diameters have been reported recently in surface-supported VLS growth at 320°C (*8*). These nanowires, which have somewhat larger diameters than those produced in the present studies, have a substantial number of kink defects. At higher growth temperatures at which straight, crystalline nanowires (comparable with the present work) are produced, the nanowire diameters are substantially larger: 40 to 100 nm.
20. J. R. Heath and F. K. LeGoues, *Chem. Phys. Lett.* **208**, 263 (1993).
21. J. Hu, X. Duan, C. M. Lieber, unpublished results.
22. We thank F. Spaepen, W. Klemperer, J. H. Chen, and R. Gordon for discussions and Y. Lu and M. Frongillo for their help in obtaining TEM data. C.M.L. acknowledges support of this work by the Office of Naval Research and the NSF Materials Research Science and Engineering Center.

10 September 1997; accepted 13 November 1997

Evidence for New Sources of NO_x in the Lower Atmosphere

Edward C. Zipf* and Sheo S. Prasad

Laboratory studies show that the reaction of short-lived $O_2(B^3\Sigma_u)$ molecules (lifetime ~10 picoseconds) with N_2 and the photodissociation of the N_2:O_2 dimer produce NO_x in the stratosphere at a rate comparable to the oxidation of N_2O by $O(^1D)$. This finding implies the existence of unidentified NO_x sinks in the stratosphere. The NO_2 observed in this experiment is isotopically heavy with a large $^{15}N/^{14}N$ enhancement. However, photodissociation of this NO_2 unexpectedly produced NO molecules with a low $^{15}N/^{14}N$ ratio. The diurnal odd-nitrogen cycle in the stratosphere will be marked by a complex isotope signature that will be imprinted on the halogen and HO_x catalytic cycles.

Recent atmospheric measurements suggest that the total O_3 removal rate in the stratosphere is determined chiefly by the HO_x and halogen catalytic cycles whose relative roles are controlled by the NO_x abundance (*1*). A key conclusion of this work is that the loss rate of ozone decreases with increasing NO_x loading in the lower stratosphere. It is therefore important to identify the sources and sinks of odd-nitrogen in the stratosphere and troposphere whose interplay determines the local NO_x abundance. Here, we report laboratory experiments showing that the photoexcitation of $O_2(B^3\Sigma_u)$ molecules and short-lived collision complexes or weakly bound N_2:O_2 dimers by the absorption of solar Schumann-Runge (SR) and Herzberg band and continuum radiation is an efficient source of NO/NO_2 in the stratosphere and possibly in the troposphere.

Figure 1 shows a diagram of the ultrahigh vacuum (UHV) system used in the photolysis experiment (*2*). Substantial amounts of N_2O and NO_x can be produced in the photolysis cell by a variety of processes that occur when synthetic air or O_2/N_2 mixtures (*3*) are irradiated with ultraviolet (UV) and vacuum ultraviolet (VUV) continuum radiation from a deuterium arc lamp (wavelength λ = 175 to 400 nm), an argon flash lamp (λ_{cutoff} ~ 115 nm), or by Hg resonance line radiation (λ = 184.95 nm) (*4*). The photolysis experiment included a Zeeman-scanned, oxygen absorption filter (*5*). This device could be used to modify the incident continuum radiation by selectively absorbing individual rotational lines of the SR bands ($B^3\Sigma_u \leftarrow X^3\Sigma_g$) from the input continuum flux while observing the effects of this subtractive process on the N_2O, NO_x, and O_3 production and loss rates.

Although the N_2O and NO_x production rates observed in this experiment were large (~1×10^{11} to 10×10^{11} molecules per second), the equilibrium mixing ratio of these species in the photolysis cell was small (<10 parts per billion by volume) because we used short irradiation times (<120 min) and a large photolysis cell to minimize wall effects. To increase the sensitivity of the apparatus, we cryogenically concentrated the N_2O and NO_x in a liquid N_2 trap (−195.8°C). The trapped NO and NO_x were subsequently separated by distillation at −100°C. We determined the efficiency of this transfer technique by introducing a 10-cm^3 sample of a standard mixture into the absorption cell directly from a calibration loop. The amount of nitrogen oxide (or oxides) in this sample was typically 1×10^{14} molecules. These tests showed that the retrieval efficiency was generally >95%; no significant wall losses were observed on the short time-scale of the irradiation experiment.

We measured the isotope composition of the NO_x in these small samples (<2 nmol) with an Extel quadrupole mass spectrometer (QMS) (1.59-cm diameter poles). The QMS was fitted with a high-efficiency electron-impact ionizer that had been developed specifically to measure the ionization cross sections of radicals and reactive atomic gases present in a source gas with a very small mixing ratio (6–8). QMS measurements of the NO/NO_2 mixing ratios showed that efficient production of NO_x occurred in the photolysis cell when air was irradiated by Hg (185 nm) radiation or by a filtered D_2 lamp (210 to 400 nm). The NO_2 yield varied linearly with the irradiation time (at fixed pressure and light intensity) (Fig. 2). These data represent a lower limit on the total NO_x production because some of the primary NO_x is converted into unmeasured higher nitrogen oxides (for example, N_2O_5) as by-products of secondary reactions and cryogenic cooling.

Surface reactions are unlikely to be the primary source of the observed NO_x because (i) no NO_x formation was observed under dark conditions; (ii) the irradiated surfaces were limited to the MgF_2 windows, which are too small in area to synthesize the observed NO_x even if we assumed that irradiated surfaces were able to do so; and (iii) although atomic oxygen is present in the system in nonnegligible amounts (at least in

E. C. Zipf, Department of Physics and Astronomy, University of Pittsburgh, Pittsburgh, PA 15260, USA.
S. S. Prasad, Creative Research Enterprises, Post Office Box 174, Pleasanton, CA 94566, USA.

*To whom correspondence should be addressed.